arXiv:1609.08432v1 [cond-mat.quant-gas] 27 Sep 2016

Electron Spin Waves in Quantum Gas of Atomic Hydrogen

L. Lehtonen,[1] O. Vainio,[1] J. Ahokas,[1] J. Järvinen,[1] S. Novotny,[1] S. Sheludyakov,[1] K.-A. Suominen,[1] S. Vasiliev,[1,*] V. Khmelenko,[2] and D. M. Lee[2]

[1]*Department of Physics and Astronomy, University of Turku, 20014 Turku, Finland*
[2]*Institute for Quantum Science and Engineering, Department of Physics and Astronomy, Texas A&M University, College Station, TX, 77843, USA*

(Dated: September 28, 2016)

We present a high magnetic field study of electron spin waves in atomic hydrogen gas compressed to high densities of $\sim 5 \times 10^{18}$ cm^{-3} at temperatures ranging from 0.26 to 0.6 K. We give a more detailed description of the experiments and analyses of data behind the discovery of electron spin waves and their BEC-like behaviour, as previously reported in PRL **108** 185304 (2012) and PRL **114** 125304 (2015).

I. INTRODUCTION

The concept of spin is one of the main features which distinguish between quantum and classical behaviour of matter. Interactions between particles having spin, obeying laws of quantum mechanics, may lead to a transport of spin variable in space and time, or propagation of the spin-perturbation in a wave-like manner. Spin waves in solid systems, e.g. ferromagnets, are usually caused by the exchange or dipolar interactions of the electrons, which have sufficient overlap of their wavefunctions. Spin waves related with nuclear spin of ^{3}He represent a special case of this phenomenon in a degenerate Fermi liquid, where a large variety of quantum effects are observed. Quantization of the spin-wave oscillations leads to a description of the system as a gas of quasi-particles, or magnons. Such quantized waves or collective excitations of particles, similar to the normal atoms, may exhibit quantum phenomena, dependent on the type of statistics they obey. For Bose-type of (quasi)particles one of the most famous is the phenomenon of Bose-Einstein condensation (BEC). Being first considered for the light quanta[1,2], statistical attraction between identical bosons leads to the macroscopic occupation of their energy ground state, when their number exceeds certain critical value for a given temperature. For cold atoms the phenomenon of BEC has been demonstrated in 1995[3,4] and has been intensively studied during last decades.

The main difficulty in the statistical treatment of the BEC of quasiparticles lie in the fact that, like for the light quanta of black body radiation, their chemical potential is zero in thermal equilibrium, and the quasiparticle number is provided by the external reservoir in amounts dictated by its temperature. Lowering the temperature decreases the occupation numbers of different quantum states including the ground state, and no criticality is reached with respect to T. Therefore, one has to consider a non-equilibrium case, when the excessive (over equilibrium) number is created by e.g. injecting quasiparticles with some external source. In such case the chemical potential becomes non-zero, and the BEC regime can be reached with macroscopic population of the ground state. Recently these effects were observed for such quasiparticles as exciton polaritons[5], triplet states in magnetic insulators[6], magnons in ferromagnets[7] and liquid ^{3}He[8], photons in a microcavity[9], and for magnons in a gas of spin-polarized atomic hydrogen (H↓)[10].

Spin waves in cold gases are fundamentally different from other systems because they occur in quantum collisions of identical particles, basically during very short time when the particles approach to the distance comparable with their degree of delocalisation in space given by the de-Broglie wavelength. Exchange effects of the particles lead to the rotation of their spins around the total spin, called Identical Spin Rotation Effect (ISR), and to a wave-like propagation of the spin perturbation. The spin waves related with ISR were first observed for the nuclear spins in the gas of ^{3}He[11] and atomic hydrogen[12], and recently for the cold gas of ^{87}Rb[13] and for electron spins of atomic hydrogen[14]. Spin waves in atomic hydrogen represent a special case because they are studied in strong magnetic fields when the nuclear and electron spins are decoupled, and each can serve as the propagating quantity.

In this paper we present a description of our experimental study of the electron spin waves in the cold gas of atomic hydrogen. The work is done in strong magnetic field of 4.6 T, and temperature range of 0.26-0.6 K, when the gas is not yet degenerate, but already sufficiently cold for studies the effects of quantum collisions. Short descriptions of our experiments was given in two Letters[10,14]. In[14] we have reported a possibility of generation of electron spin waves, guiding and trapping them with magnetic potential. In[10] an emergence of spontaneous coherence and BEC-like behaviour was observed. Here we will present more detailed description of the experimental apparatus and technique, further analysis of the experimental results, and theoretical modelling of the magnons behaviour.

II. BACKGROUND

A. ISR effect

The nature of the ISR effect requires for the gas to be in the quantum regime. The gas is considered to be quantum when the thermal de-Broglie wavelength Λ_{th} substantially exceeds the scattering length of elastic collisions a_s. The quantum gas condition is not an equal concept with the degenerate quantum gas. The latter situation occurs when Λ_{th} exceeds the mean interatomic spacing r, and it is associated with drastic changes in the macroscopic properties of the gas; the phenomenon of BEC of atoms. Therefore, there exists a rather wide experimentally accessible range of densities $n \sim r^{-3}$ and temperatures where $r > \Lambda_{th} > a$, i.e. the gas is in the quantum regime but not yet degenerate. The rapid progress to BEC with alkali atoms has left this parameter region quite neglected. This range is especially large for H because of the small size of the atom ($a_H \approx 0.07$ nm). In the quantum gas regime there appears a special type of collisions when identical particles exchange (rotate) their spins without changing their momentum. Such Identical Spin Rotation effect was predicted by Bashkin[15] and Lhuillier and Laloe[16]. Accumulating in multiple subsequent collisions ISR may lead to the propagation of spin waves. Efficiency of ISR depends on the ratio of the frequencies of spin changing collisions to the elastic collisions and is given by the so-called ISR quality factor $\mu^* \sim \Lambda_{th}/a_s$, which is large in the quantum gas regime.

Soon after their theoretical prediction spin waves of ISR type were observed for spin-polarized 3He gas in Paris[11], and for nuclear spins of atomic hydrogen gas in the experiments of David Lee at Cornell University[12]. Progress in trapping and cooling of alkali vapours allowed observation of the ISR waves also for ultracold ^{87}Rb[13]. In all above mentioned experiments the spin waves were associated with nuclear spins (H protons and ^{3}He) or with the total spin of atoms in zero magnetic fields (^{87}Rb). Pure electron spin waves were observed for atomic hydrogen in strong magnetic fields[14], and are considered in this work.

B. Spin waves in quantum gases

The dynamics of spin waves in quantum gases is described by the ISR equation[16].

$$\frac{\partial M_+}{\partial t} = \left(\frac{D_0}{1 + i\epsilon\mu^* M_0} \nabla^2 - i \overbrace{\gamma H_z}^{iV(r)} \right) M_+ \qquad (1)$$

Here $M_+ = M_x + iM_y$ with $\vec{M} = (M_x, M_y, M_z + M_0)$, $M_x, M_y, M_z \ll M_0$ being the spin polarization vector, $\epsilon = 1$ for bosons and -1 for fermions, H_z the external magnetic field in z-direction, γ the gyromagnetic ratio of electron or nucleus involved, D_0 the axial spin diffusion coefficient, and μ^* the spin wave quality factor. Multiplying the equation with i gives a Schrödinger-like equation with damping. The kinetic energy is, as would it be for a particle with effective mass $m^* \approx -\hbar\mu^*/2D_0\epsilon$, and the potential term is defined by the Zeeman energy of the spin in the magnetic field H_z. This analogy allows treatment of the ISR magnons in a manner similar to the real atoms, trapped in a magnetic bottles. We may use similar terminology to that used in the cold atoms field, and classify the magnons as high and low field seekers. For electrons γ_e is negative, which leads to trapping of the electron spin waves in the maximum of magnetic field, making their behavior similar to the high field seeking atoms. For protons γ_p is positive, which makes the nuclear spin magnons low field seekers, with the effects of the potential for them being 650 times weaker. However, there is one important difference in the trapping of the magnons. It turns out to be possible to use the walls of the experimental chamber as a part of the trap. With a special choice of non-magnetic materials for the walls (e.g. liquid helium) one may realize nearly perfect reflective boundary conditions for the spin waves. Then, the combination of such walls with the magnetic field maximum allows building 3D trap for high or low- field seeking magnons.

The ISR theory can be applied to any internal degree of freedom of colliding atoms, which is exchanged in the quantum collisions. It can be nuclear or electron spin, a pseudo-spin, or just some quantity, which makes atoms distinguishable. But it turns out that there is fundamental difference in the sense of the identical spin rotation, which depends on the type of the atoms and the spin involved. This is taken into account by two other parameters ϵ and μ^* (or actually on their product $\epsilon\mu^*$ in the equation 1. The value of μ^* depends on the details of interatomic potential, and basically on the sign of the s-wave scattering length in the limit of cold collisions. It has been evaluated that for atomic hydrogen μ^* is large and negative, while for ^{3}He it is positive at lowest temperatures, but changes sign at around 0.5 K[16]. Then, since atomic hydrogen obeys bosonic statistics with $\epsilon = 1$, the kinetic energy term for the H magnons, like for normal atoms, implies positive effective mass. The situation is different for fermionic deuterium, which changes the sign ϵ and of the kinetic term. For ^{3}He the $\epsilon\mu$ product is positive, while γ_n is negative, implying low field seeking behaviour with negative effective mass. It follows from this discussions that the dynamics of ISR magnons for above mentioned gases may be completely different and reveal new and interesting features.

C. BEC-like behaviour of magnons in quantum gases

Quantized waves or collective excitations of particles obey Bose statistics, and may exhibit quantum phenom-

ena similar to BEC. Statistical attraction leads to the macroscopic occupation of their energy ground state, when their number exceeds certain critical value. However, the difference in the statistical treatment of the BEC of quasiparticles lie in the fact that, like for the light quanta of black body radiation, their chemical potential is zero in thermal equilibrium, and the quasiparticle number is provided by the external reservoir in amounts dictated by its temperature. Lowering the temperature decreases the occupation numbers of different quantum states including the ground state, and no criticality is reached with respect to T. Therefore, one has to consider a non-equilibrium case, when the excessive (over equilibrium) number is created by e.g. injecting quasiparticles with some external source. In such case, the chemical potential becomes non-zero, and the BEC regime can be reached with macroscopic population of the ground state. These effects were observed for several systems of quasiparticles of completely different nature[5–10]. Low effective masses of magnons, of the order of electron mass, make achievement of BEC possible even at room temperature[7].

BEC-like behavior, or spontaneous coherence, in systems of coupled oscillators has been predicted by Fröhlich[17] and is often referred to as the Fröhlich coherence.

Further insight into the behaviour of quasiparticles under pumping is obtained from the work of Bugrij and Loktev[18], who demonstrated that pumping magnons into the system leads to the preferential population of the ground state.

III. EXPERIMENTAL DETAILS

A. Apparatus

Identical spin rotation is a weak effect, and spins are rotated by a small angle in each spin-changing collision. Therefore, in order to get the total angle changed significantly, atoms need to make many hundreds of such collisions before they traverse the sample cell from one end to another. Since the effective mean free path for spin changing collisions can be estimated as $\lambda_{SE} \sim 1/(n\Lambda_{th}^2) \sim 10\mu$m, at the gas density of 10^{16} cm^{-3} and temperature of 0.3 K, one can estimate that for the sample cell size of 0.5 mm the atom on the average 50 spin-changing collisions during its travel between the SC walls. Therefore, the gas densities substantially higher than that are required to observe ISR spin wave modes. So high densities cannot be reached with the standard trapping techniques used in BEC experiments with alkali vapours. Therefore, we utilize the old conservative compression technique by reducing the volume of the sample surrounded by physical rather than magnetic walls. Presence of the physical walls in experiments with atomic hydrogen is the main obstacle for reaching high densities of the gas because of the adsorption and subsequent recombination of atoms on the surface. Superfluid helium turned out to be the material with smallest adsorption energy of ∼1 K, and therefore, all experiments with high density H gas have to be done in the sample cell covered by superfluid helium and at temperatures above ∼300 mK. For spin waves, however, the physical wall just provides a reflective boundary and does not impose any extra losses. Therefore, combination of the magnetic field maximum with the helium covered wall can form a potential well where the spin wave modes described by the equation (1) can be excited and trapped. Several other requirements specific to this experiments are: the strongly inhomogeneous RF field on the scale of the H sample size, linear response of the detection system to the magnetic resonance, and control of the magnetic field profile serving as the potential energy for magnons in Eq. 1. These features are implemented in the compression cell depicted in Fig. 1 a.

The electron spin wave experiments with atomic hydrogen gas were conducted in a cryostat with home made dilution refrigerator equipped with cryogenic electron spin resonance (ESR) spectrometer[19]. Recently the spectrometer has been modified to operate also in the pulsed mode. In this work both CW and pulse mode spectra are presented. Applying shaped pulse excitation allowed probing the sample selectively. Furthermore, in the pulsed mode the spectra could be collected with intervals of the order of 0.2-0.5 sec, which provided possibility of recording substantially faster processes than in CW mode. This was essential for the last stage of the decay of the H gas when it evolved into the bubble with rapidly changing size and density. The experimental cell where the compression and detection of magnons in H gas was performed is shown in Fig. 1. It is located inside a superconductive magnet in a magnetic field of 4.6 T. In this field the frequency of the ESR-resonance is around 130 GHz.

In the course of spin wave experiments we measured spectra in three distinct experimental cells. The most essential difference between these cells was the material around the detection region at the top of the of the sample volume, i.e. the volume into which the evanescent tail of the rf-field used for ESR penetrates from a Fabry-Perot cavity. The slight magnetization of this surrounding material and the consequent inhomogeneities in the magnetic field amplitude proved to be of fundamental importance for the discovery of the trapped spin wave modes reported in[14].

In all these three experimental cells, the atomic hydrogen sample gas was compressed into a small diameter cylindrical volume from a larger volume into which it is accumulated in the beginning of an experiment cycle. The sample volume is separated from the FP-cavity with a gold coated kapton film, which prevents the hydrogen from leaking into the high amplitude ESR-volume inside the cavity. The gold coating acts as the planar mirror of the cavity and allows the rf-field to interact with the sample through a sub-critical (0.4 mm) whole in the gold coating, centred with the sample volume. This construc-

tion produces a highly inhomogeneous rf-field in the sample volume, with a characteristic $(1/e)$ penetration length of ≈ 80 μm into the sample volume. An inhomogeneous ESR-excitation is crucial for the excitation of spin wave modes.

The first generation experimental cell had an all-copper construction and the slight diamagnetic magnetization of copper modified the spectra in a manner which later proved to be characteristic for trapped spin wave modes. The sample preparation in the all-copper cell suffered from overheating, as there was no efficient path for the recombination heat to escape the sample volume, and therefore a second generation experimental cell was designed with an additional liquid helium cooling volume surrounding the sample volume. The sample volume of the second generation sample cell had an all plastic construction around its excitation and detection region, in order to minimize magnetization induced disturbances, as they were considered at the time. The liquid helium coolant, connected to the mixing chamber, the coldest part of the cryostat, proved to be highly functional and it allowed compressing the atomic hydrogen gas to exceedingly high pressures. Unfortunately, due to the delicate, plastic construction, a liquid helium leak developed between the sample and coolant volumes, allowing the helium piston liquid to escape to the coolant volume. Therefore, the third generation sample cell was designed to have more robust junctions between the two volumes. Especially, the uppermost seal between the sample volume and the coolant volume was glued with a 0,5 mm meniscus of Stycast 1266, preventing the possibility of another leak between the volumes. Unknown to us at the time of designing, also Stycast turned out to be slightly diamagnetic at extremely low temperatures. The fraction of a Gauss magnetization gave rise to modifications in the spectra similar to those seen with the first generation copper cell, but this time more localized and therefore more controllable with the setup's gradient coils. Combining the information from measurements recorded with all these three experimental cells helped us understand the nature of the trapped spin-wave modes[14].

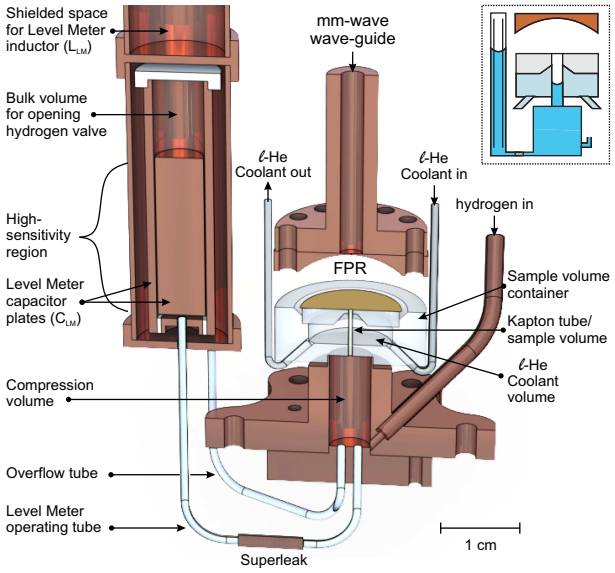

FIG. 1. Cross section of the experimental cell. Helium piston reservoir with level meter capacitor, FP resonator for ESR, coolant helium volume and tubes, hydrogen gas sample accumulation volume and fill line, compression volume and excitation region.

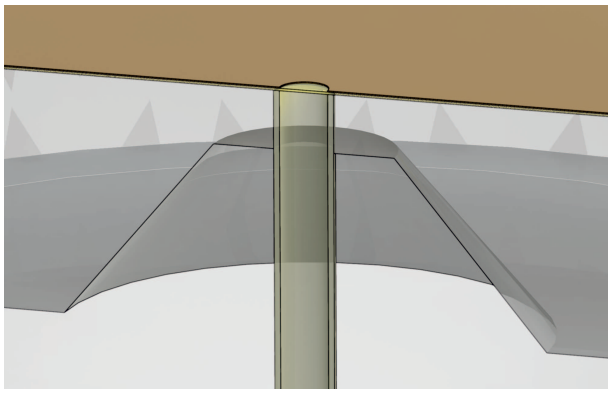

FIG. 2. Magnified cross section of the experimental cell around the top part of the sample volume (cylidrical volume in the centre). Also visible are the stycast meniscus, gold coated mirror of the Fabry-Perot resonator and the coupling hole in the gold coating above the sample volume, and the top part of the helium coolant volume.

B. Procedure

A liquid helium piston was used to compress the hydrogen gas in order to reach high densities. The hydrogen gas was first loaded into a larger volume, using the liquid helium piston as a valve opening and closing the hydrogen gas loading inlet.

The liquid helium piston was operated by adjusting a temperature difference (ΔT) between two sides of a super leak. On the reservoir side of the piston the liquid helium was stored between coaxially aligned capacitor plates. Above the inner capacitor plate was a larger bulk volume, which allowed emptying the compression volume for loading a hydrogen gas sample. The capacitor was part of an LC-circuit driven by a tunnel diode circuitry. The operating frequency of ≈ 25 MHz of this LC-oscillator was detected at room temperature. The frequency difference between empty and full (of liquid helium) capacitor was $\approx$ 190 kHz and with our usual sampling rate of 0.5 Hz the detection accuracy was a few Hertz. This gave us a volume resolution of approximately 1 nl corresponding to a helium level change of $\approx 0.2\,\mu$m in the sample volume.

A typical experiment cycle lasted ≈ 1500 seconds and consisted of five distinctive stages: I Accumulation, II Pre-compression, III Pause, IV Final compression and V Sample Decay.

The recording of spectra started already during the accumulation stage I with low hydrogen gas densities, while ISRE-induced spin dynamics were still absent. These purely lorentzian shaped absorption (and dispersion) spectra measured between the high density spin wave spectra served calibration against long term frequency/magnetic field drifts.

During pre-compression the hydrogen gas density was increased, but as the initially accumulated sample gas included both a- and b-state atoms a pause in the compression sequence was found to be necessary, in order to let the a-state atoms exit the sample gas via recombination. A too fast compression with a-state atoms in the sample lead to a runaway recombination and explosion of the sample. After few tens of seconds of steady state evolution, the final compression stage was initiated, raising the temperature difference between compression and reservoir volumes to a desired value. The range of possible final compression forces was large leading to a large range final hydrogen gas densities, although too strong compressions again induced a runaway recombination, irrespective of the pause before the final compression.

During the compression the geometry of the sample volume is constantly changing, as the upper meniscus of the liquid helium piston rises in the volume, pushing the hydrogen gas towards the top of the volume. As most of the detectable spin wave dynamics is happening at the top most mm of the sample volume, the helium piston induced geometry changes affect the spectra only at the very end of a sufficiently strong compression. During weak compressions the piston does not reach the top of the sample volume. For the weak compression, the highest hydrogen gas densities occur at the end of the compression volume heating ramp, after which the hydrogen gas density starts to decrease due to recombination and ending with a vacuum above the piston. The most accurate hydrogen gas density measurements we could perform during the period of constant ΔT between the volumes, when the hydrogen gas density is declining. The density dependence of the spin wave dynamics in a cylindrical geometry, and with a toroidal potential minimum for the magnons, was seen twice during these compressions. Once while the density is increasing during the final compression, and in reversed order during the decay of the sample.

At the end of relatively strong final compressions the hydrogen gas collapsed into a bubble immersed in liquid helium at the top of the sample volume. The bubble stage of the compression usually lasted few tens of seconds, during which we could measure tens spectra. Although we were capable of measuring the volume changes relatively accurately even during final seconds of the bubble life-time, determining the hydrogen pressure turned out be non-trivial. In contrast to the weaker compression, the hydrogen density is monotonously increasing during the evolution of the bubble.

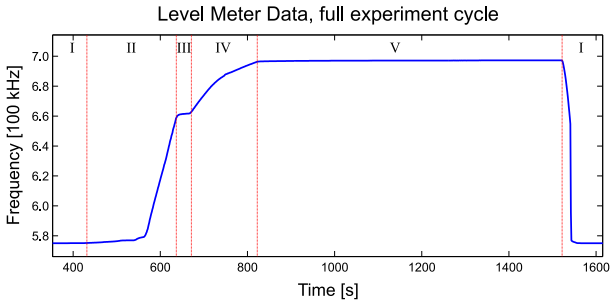

FIG. 3. Level meter data for a full experiment cycle

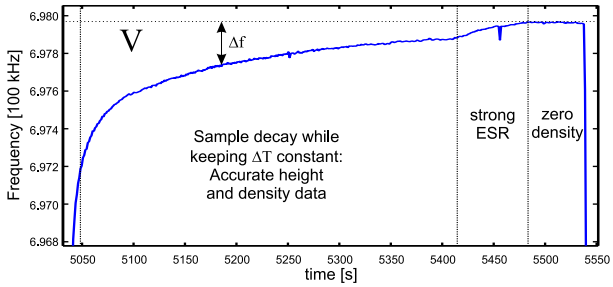

FIG. 4. Level meter data detail for sample decay

C. Magnetic Field Gradients

The total magnetic field inside the sample volume is a sum of fields from several independent sources. The overall direction of the field is set by the main coil of the superconductive magnet, creating the 4,6 Tesla polarizing field. In our experiments this polarizing field is parallel to the symmetry axis of the experimental cell and points. A strong magnetic field is needed to maintain the spin-polarization of the hydrogen atoms. Spin polarization is necessary as it significantly slows down the recombination into molecular hydrogen, allowing experiments with atomic hydrogen.

Magnetic fields from all other sources, including the build in shim, gradient, and sweep coils of the main magnet, are much weaker than the main coil field, but have a significant role in fine tuning the total field amplitude and modulating the amplitude gradients. In addition to the built-in coils i the main magnet, we had altogether 5 external coils, out of which two were in a Helmholtz configuration, and other two in an anti-Helmholtz configuration. Due to the large difference in field amplitudes between the main coil and the field from the rest of the coils, only the field component parallel to the main coil field affects the total field amplitude. The transversal components introduce only a vanishingly small tilt to the direction of the total magnetic field.

Besides the magnetic field from the externally controlled coils, also magnetized material in the vicinity of the sample volume affects the total magnetic field amplitude. In these experiments the slight diamagnetic magnetization of the epoxy (Stycast 1266) collar around the

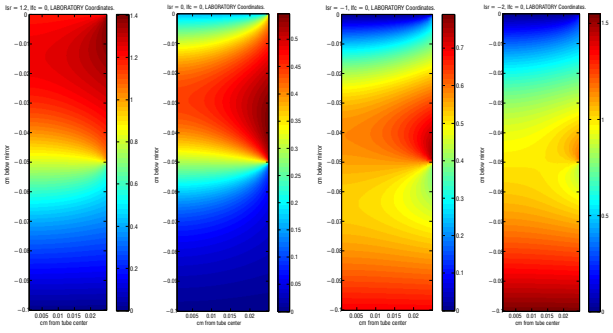

FIG. 5. Half cross-sections of magnetic field amplitudes near the top of the sample volume for four different gradient coil current values. The added gradient field is homogeneous in radial direction, adding only a variable, linear gradient in z-dircetion. The local magnetic field maximum (dark red) at the outer wall of the sample volume moves both spatially and in relative field strength compared to the excitation and detection region at the top of the volume.

top of the sample volume created a toroidal magnetic field maximum at the outer wall of the sample volume. The location and relative strength of this maximum, compared to the magnetic field at the excitation region at the top center of the sample volume, was controllable by varying the vertical field gradient via coils. In fig. 5 the simulated magnetic field amplitude for four different gradient coil currents is shown.

IV. SOLUTIONS OF THE ISR EQUATION IN TOROIDAL GEOMETRY

The ISR equation can be solved numerically based on the magnetic potentials presented in fig. 5. However, it turns out that with certain approximations for the magnetic field function it is possible to solve it also analytically. Since the structures and types of the spin wave modes are better understood in the latter case, in this section we will present analytic solutions of the ISR equation 1 using the approximation for the spatial dependence of the magnetic field in the trapping region of the form $\vec{H}(r,z) = \left(H_0 + H_r r^2 - H_z z^2\right)\hat{\mathbf{e}}_z$ with $\mu_0 H_0 = 4.6\,\mathrm{T}$, $\mu_0 H_r = 24\times10^{-3}\ \mathrm{T/c^2m}$, and $\mu_0 H_z = 6.0\times10^{-3}\,\mathrm{T\,cm^{-2}}$. The ISR equation has a separable solution $M_+(t,r,z,\theta) = e^{i\omega t}R(r)Z_{p,o}(z)e^{ik\theta}$ in terms of confluent hypergeometric functions:

$$
\begin{aligned}
R(r) &= r^k e^{-\frac{r^2\sqrt{i-\mu}}{2\lambda_r^2}}\,{}_1F_1\left(\begin{matrix}\frac{k+1}{2}+\Omega_l^k\\ k+1\end{matrix};\frac{r^2}{\lambda_r^2}\sqrt{i-\mu}\right)\\
Z_e(z) &= e^{-\frac{z^2}{2\lambda_z^2}\sqrt{\mu-i}}\,{}_1F_1\left(\begin{matrix}\Gamma_e+\frac{1}{4}\\ \frac{1}{2}\end{matrix};\frac{z^2}{\lambda_z^2}\sqrt{\mu-i}\right)\\
Z_o(z) &= z e^{-\frac{z^2}{2\lambda_z^2}\sqrt{\mu-i}}\,{}_1F_1\left(\begin{matrix}\Gamma_o+\frac{3}{4}\\ \frac{3}{2}\end{matrix};\frac{z^2}{\lambda_z^2}\sqrt{\mu-i}\right)
\end{aligned}
$$

In the axial direction there are both even and odd solutions; the complete solution can be specified with (k,l,m,p), where k specifies the azimuthal mode, l the radial, m the axial, and p whether the solution is even or odd.

We approximate that there is no spin flow into the boundary at the boundary. This translates to Neumann boundary condition $\left.\frac{\partial M_+}{\partial\vec{n}}\right|_{\partial V} = 0$; in our case at $z = 0.5\,\mathrm{mm}$ and $r = 0.25\,\mathrm{mm}$. This gives three characteristic equations, one in the radial direction and two in the axial, for the even and odd solutions (see Appendix A for details). These equations can be numerically solved for Ω_l, Γ_m^p to give the modes and the complex eigenfrequency ω.

$$
\begin{aligned}
\omega =& \frac{D_0}{(-\mu+i)^{\frac{1}{2}}}\\
&\times\left(\frac{(-\mu+i)^{\frac{1}{2}}}{\lambda_0^2}+4\left[\frac{i\Gamma_m^p}{\lambda_z^2}-\frac{\Omega_l^k}{\lambda_r^2}\right]\right)\\
\lambda_{r,z} =& \left(\frac{D_0}{H_{r,z}|\gamma|}\right)^{\frac{1}{4}},\ \lambda_0 = \left(\frac{D_0}{H_0|\gamma|}\right)^{\frac{1}{2}}
\end{aligned}
$$

A. Characteristics of Magnons

As in the case of a particle in a finite potential, the magnon spectrum splits into two branches: trapped and 'free'. The split is readily noticeable in fig. 6, where the behaviour of the roots of the characteristic equations changes at the cusp of the curve. The change can also be seen in the mode functions fig. (7), in general as an increasing amplitude where it was zero before. For hydrogen, these are the axis and the ends of the cylinder.

The fact that the magnons of hydrogen are high-field seekers is evident from fig. 6, where for hydrogen there is a highest frequency (corresponding to highest magnetic field via $\omega = \gamma B$). The mode functions (R_0^0, Z_0 in fig 7) are also concentrated in areas of strong magnetic field.

Evaluating imaginary part of the frequencies ω for each mode gives their damping rates, and characteristic lifetime of the modes. The magnon decay times are presented in fig. 6). These evaluations are in reasonable agreement with experiment.

One would expect decay times to decrease as a function of mode number, and generally this seems to be case. However, there are some curious exceptions to the rule: The $(0, l = 6, 0, \mathrm{even})$ mode, with frequency close to the saddle point at $\frac{\gamma B_0}{2\pi}$, has a lifetime longer than many higher frequency modes ($\tau = 17.11\,\mu\mathrm{s}$, being the 17th longest-lived mode, while $(0, l = 3, 0, \mathrm{even})$ is 27th). This mode seems to be concentrated in the center of the cylinder in both radial and axial directions (see figure 7).

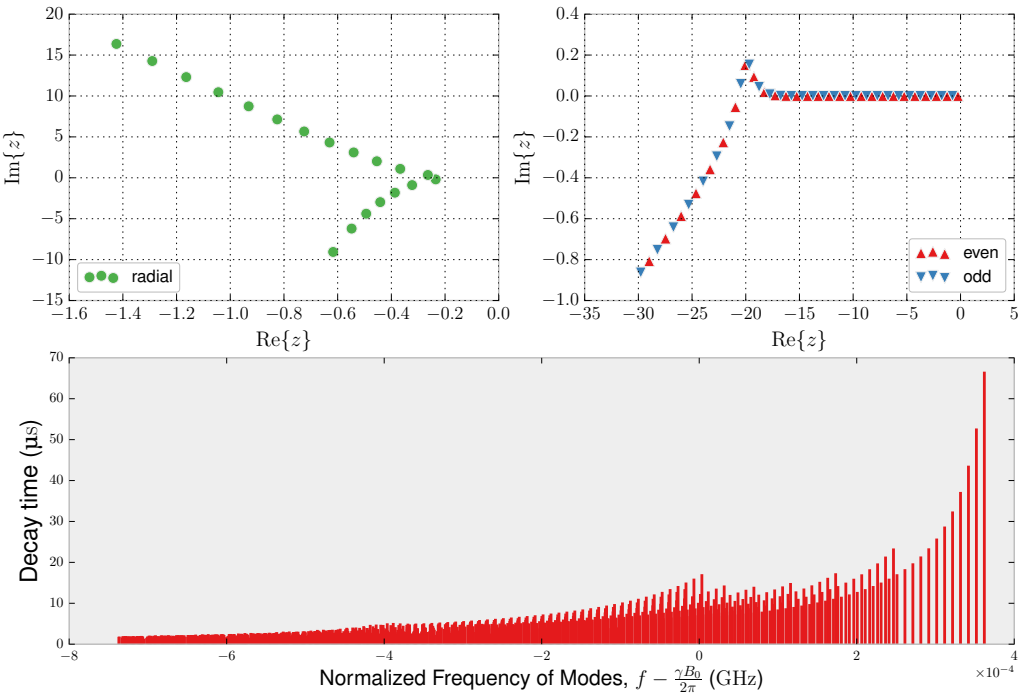

FIG. 6. Solutions of Characteristic Equations and Mode Frequencies ($\rho = 2 \times 10^{17}\,\mathrm{cm}^{-3}$, $T = 0.25\,\mathrm{K}$)

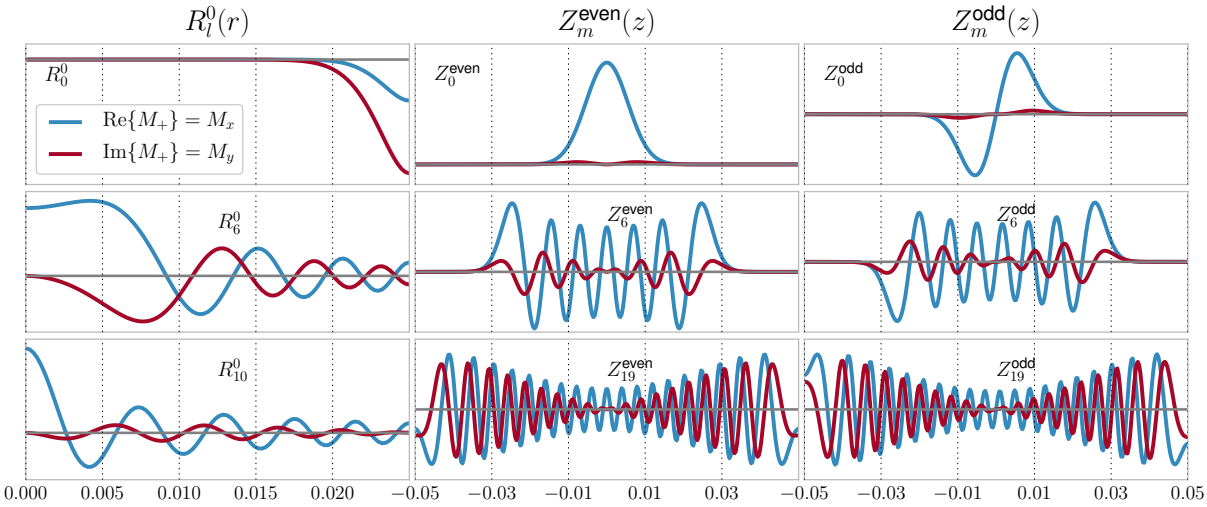

FIG. 7. Eigenmodes $R^0_{0,6,10}, Z^{\mathrm{even,\ odd}}_{0,6,19}, Z^{\mathrm{even,\ odd}}_{0,6,19}$

V. RESULTS

A. Bubbles

During the experiment the hydrogen gas is continuously depleted through recombination through a variety of mechanisms, most significant being surface recombination with hydrogen adsorbed on the surrounding helium. The recombined hydrogen molecules then quickly escape into the surrounding helium bath. When enough of the gas has been lost, the gas column may collapse into a bubble, an event clearly visible in the change of the absorption spectrum (fig. 8). The volume of the bubble is readily accessible from level meter data, this is not the case for the rest of the thermodynamic variables such as

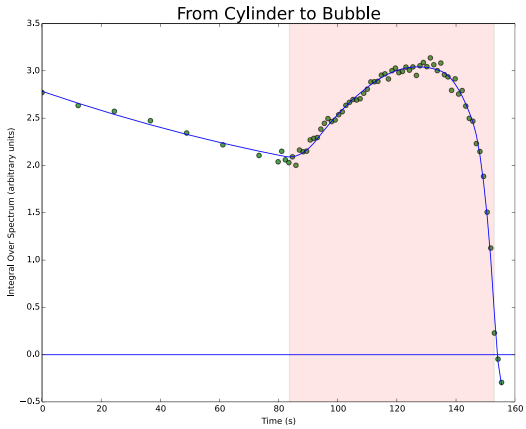

FIG. 8. Cylinder to Bubble Transition
Area of the absorption peak is proportional to the density of atomic hydrogen. A clear transition from a cylindrical geometry to a bubble is seen.

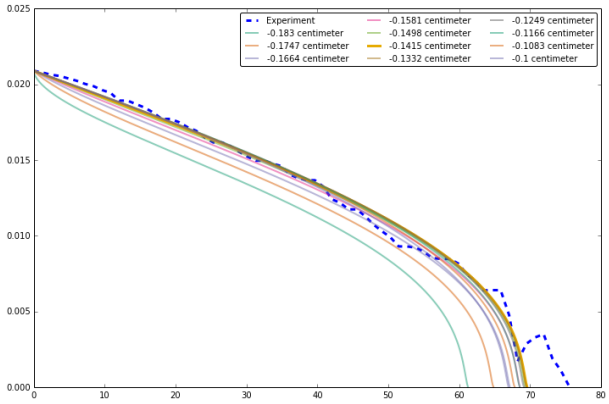

FIG. 9. Fitting Bubble Simulation to Experiment
Simulations of the bubble radius (cm) with hydrostatic pressure/height of helium column as fitting parameter. Best fit (in bold) was chosen using minimal squared difference from the level meter data, and turns out to exert a negative pressure on the bubble.

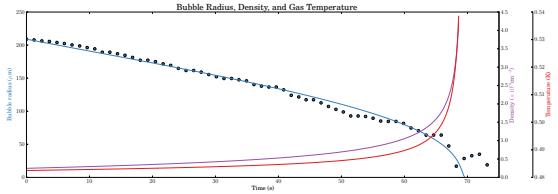

FIG. 10. Bubble thermodynamics

number density and temperature. Hence the necessity for simulating the bubble's dynamics.

The simulations are based on similar work done earlier[20]. The basic scheme is as follows: First, the number of each of the four hyperfine states evolves according to coupled rate equations (see supplementary material) which account for different recombination and relaxation mechanisms. Recombination results in heating and loss of atomic species. Heating together with cooling due to the helium bath at the boundary of the bubble establish a temperature profile in the gas, which in turn affects the reactions rates in different parts of the gas. Heating and losses also change the volume so as to counter the bubble's surface tension $\frac{2\sigma(T)}{r}$. For more details refer to supplementary material and[20].

Results of the simulation are shown in fig. 9. Height of the helium column causing hydrostatic pressure was used as the fitting parameter. The corresponding density and temperature in the bubble are shown in fig. 10. Both of them rise sharply during the final moments of the bubble's existence. For density this is expected as the surface tension of the bubble is proportional to $\frac{1}{r}$; the heating at the end is rather dramatic and may be spurious.

B. FID Analyses

One of the striking the features in the evolution of the free induction decays signals (fig 11 (b)) is the development of a node as the density of hydrogen gas increases. This immediately suggests an interpretation in terms of a rapidly-decaying component, followed by another component which first grows, then decays. One such possible model is given by

$$\begin{cases} A_1 e^{-\frac{t}{\tau_1}} \sin(\omega t) + A_2 \sin\left(\frac{t}{\lambda}\right) \sin(\omega t) & a < t \\ A_1 e^{-\frac{t}{\tau_1}} \sin(\omega t) + A_2 \sin\left(\frac{a}{\lambda}\right) e^{-\frac{t-a}{\tau_2}} \sin(\omega t) & a \geq t \end{cases} \tag{2}$$

For smoothness of the model, it is natural to require the continuity of the function and the first derivative. This may be used to determine $a = a(\lambda, \tau_2)$)

However, working with such a model one quickly realizes that the node of the signal is sometimes surprisingly thin and steep, unlike what the simple model can produce. A possibility, confirmed by the Fourier spectrum (the dip in fig. 11 (a)), is that the node is a result of destructive interference of two signals with a phase difference of about $\frac{\pi}{2}$.

The presence of interference opens other possibilities beyond the apparent decay-revival scenario. Namely, a signal of the form

$$A_1 e^{-\frac{t}{\tau_1}} \sin(\omega t) + A_2 e^{-\frac{t}{\tau_2}} \sin\left(\omega t + \frac{\pi}{2}\right) \tag{3}$$

can also produce an FID envelope seen in the data. Indeed the envelope can be decomposed in multiple ways, though they may not produce exactly the same signal. In practice our best fits to experimental data in both FID and Fourier spaces are insufficient to distinguish between the decay-revival model and eq. 3 (fig. 11 (a) and

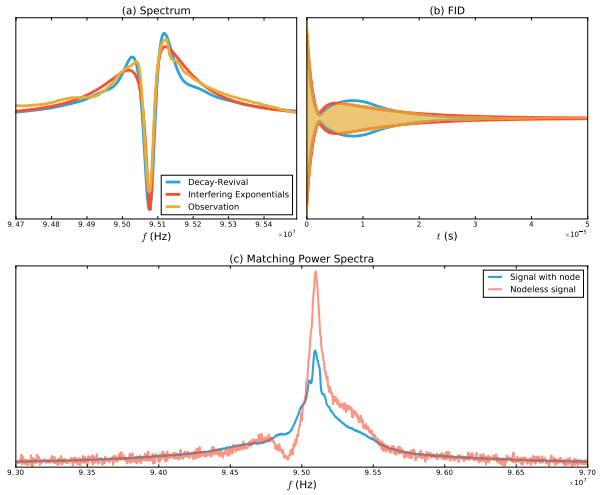

FIG. 11. (a) Comparison of Fourier spectra of models with experiment. (b) Comparison of free induction decay curves. (c) Matching power spectra from two different measurements, to get an estimate of the scaling due to hydrogen density difference.

(b)). Yet, a 'fine-tuning' argument can be made in favor of interference: the beginning of the revival is so closely fine-tuned to the vanishing of the decaying signal that it's more likely for destructive interference to play a role.

One way to approach the problem of multiple decompositions is to assume that the FIDs of different densities share common features. Specifically, the exponential decay of the incoherent signal is present in all FIDs with magnitude determined by density. It is assumed that higher density results in an amplification of the FID signal (due to more spins being excited), effectively multiplying it with some constant. Under this assumption one may compare the spectra without a node to those with one, and subtract the nodeless signal scaled by some constant (fig. 11 (c)) .

Determining the constant from the FID is largely a matter of taste, but the Fourier power spectrum provides a way to do it by matching the tails of the central peak (the central peak itself has more structure which can't be matched). Even then the goodness of the fit depends on the interval which is used for the matching, leaving some uncertainty into the value of the constant. Varying the constant slightly typically does not cause very great changes, though it may result in some small artefacts mainly at the beginning of the difference of the FID signals.

ACKNOWLEDGMENTS

This work was supported by the Academy of Finland (Grants No. 122595, and 133682) and the Wihuri Foundation.

VI. APPENDIX A. CHARACTERISTIC EQUATIONS

The characteristic equations impose the boundary conditions on the modes and allow solving for $\Omega_l^k, \Gamma_m^{\text{even, odd}}$. For hydrogen these are

$$R^2\sqrt{-\mu+i}\,(2\Omega+k+1)\,{}_1F_1\left(\begin{matrix}\Omega+\frac{k+3}{2}\\ k+2\end{matrix};\frac{R^2}{\lambda_r^2}\sqrt{-\mu+i}\right)$$
$$+(k+1)\left(k\lambda_r^2-R^2\sqrt{-\mu+i}\right){}_1F_1\left(\begin{matrix}\Omega+\frac{k+1}{2}\\ k+1\end{matrix};\frac{R^2}{\lambda_r^2}\sqrt{-\mu+i}\right)=0$$

$$(4\Gamma_e+1)\,{}_1F_1\left(\begin{matrix}\Gamma_e+\frac{5}{4}\\ \frac{3}{2}\end{matrix};\frac{L^2}{\lambda_z^2}\sqrt{-(-\mu+i)}\right)-{}_1F_1\left(\begin{matrix}\Gamma_e+\frac{1}{4}\\ \frac{1}{2}\end{matrix};\frac{L^2}{\lambda_z^2}\sqrt{-(-\mu+i)}\right)=0$$

$$\frac{L^2}{3}(4\Gamma_o+3)\sqrt{-(-\mu+i)}\,{}_1F_1\left(\begin{matrix}\Gamma_o+\frac{7}{4}\\ \frac{5}{2}\end{matrix};\frac{L^2}{\lambda_z^2}\sqrt{-(-\mu+i)}\right)+\left(\lambda_z^2-L^2\sqrt{-(-\mu+i)}\right){}_1F_1\left(\begin{matrix}\Gamma_o+\frac{3}{4}\\ \frac{4}{2}\end{matrix};\frac{L^2}{\lambda_z^2}\sqrt{-(-\mu+i)}\right)=0$$

* servas@utu.fi

[1] S. N. Bose, Zeitschrift für Physik A Hadrons and Nuclei **26**, 178 (1924).
[2] A. Einstein, Sitzungsber. Kgl. Preuss. Akad. Wiss. **261** (1924).
[3] M. H. Anderson, J. R. Ensher, M. R. Matthews, C. E. Wieman, and E. A. Cornell, Science **269**, 198 (1995).
[4] K. B. Davis, M.-O. Mewes, M. R. Andrews, N. J. van Druten, D. S. Durfee, D. M. Kurn, and W. Ketterle, Physical Review Letters **75**, 3969 (1995).

[5] J. Kasprzak, M. Richard, S. Kundermann, A. Baas, P. Jeambrun, J. M. J. Keeling, F. M. Marchetti, M. H. Szymańska, R. André, J. L. Staehli, V. Savona, P. B. Littlewood, B. Deveaud, and L. S. Dang, Nature **443**, 409 (2006).
[6] C. Rüegg, N. Cavadini, A. Furrer, H.-U. Güdel, K. Krämer, H. Mutka, A. Wildes, K. Habicht, and P. Vorderwisch, Nature **423**, 62 (2003).
[7] S. O. Demokritov, V. E. Demidov, O. Dzyapko, G. a. Melkov, a. a. Serga, B. Hillebrands, and a. N. Slavin, Nature **443**, 430 (2006).
[8] S. Autti, Y. M. Bunkov, V. B. Eltsov, P. J. Heikkinen, J. J. Hosio, P. Hunger, M. Krusius, and G. E. Volovik, Phys. Rev. Lett. **108** (2012), 10.1103/physrevlett.108.145303.
[9] J. Klaers, J. Schmitt, F. Vewinger, and M. Weitz, Nature **468**, 545 (2010).
[10] O. Vainio, J. Ahokas, J. Järvinen, L. Lehtonen, S. Novotny, S. Sheludiakov, K.-a. Suominen, S. Vasiliev, D. Zvezdov, V. V. Khmelenko, and D. M. Lee, Physical Review Letters **114**, 125304 (2015).
[11] P. J. Nacher, G. Tastevin, M. Leduc, S. B. Crampton, and F. Laloë, Journal de Physique Lettres **45**, 441 (1984).
[12] B. R. Johnson, J. S. Denker, N. P. Bigelow, L. P. Lévy, J. H. Freed, and D. M. Lee, Physical Review Letters **52**, 1508 (1984).
[13] J. M. McGuirk, H. J. Lewandowski, D. M. Harber, T. Nikuni, J. E. Williams, and E. A. Cornell, Physical Review Letters **89**, 90402 (2002).
[14] O. Vainio, J. Ahokas, S. Novotny, S. Sheludyakov, D. Zvezdov, K.-A. Suominen, and S. Vasiliev, Physical Review Letters **108**, 185304 (2012).
[15] E. P. Bashkin, JETP Letters **33**, 8 (1981).
[16] C. Lhuillier and F. Laloë, Le Journal de Physique **43**, 197 (1982).
[17] H. Fröhlich, Physics Letters A **26**, 402 (1968).
[18] A. I. Bugrij and V. M. Loktev, Low Temperature Physics **34**, 992 (2008).
[19] S. Vasilyev, J. Järvinen, E. Tjukanoff, A. Kharitonov, and S. Jaakkola, Review of Scientific Instruments **75**, 94 (2004).
[20] T. Tommila, E. Tjukanov, M. Krusius, and S. Jaakkola, Physical Review B **36**, 6837 (1987).